3. Device Examples

3.1 Model Confirmation

Appendix A gives three simple examples that verify different types of SimWindows calculations. These are just a few of the many types of devices that can test the operation of SimWindows. The first example uses a simple Si pn diode to compare the electric field from SimWindows with the electric field computed using the complete depletion approximation. The second example compares the short circuit current of a GaAs photodetector using SimWindows and an analytical expression. The last example uses a simple semiconductor resistor to compare the lattice temperature from SimWindows with a temperature computed analytically. Although there are slight differences in each of the comparisons, these simple cases demonstrate that different features in SimWindows are functioning properly. The following sections present in depth simulation results for two complex devices.

3.2 Vertical Cavity Surface Emitting Laser

The most sophisticated device that SimWindows simulates is the vertical cavity surface emitting laser (VCSEL). This device utilizes most of SimWindows' capability and is a good demonstration of how the program integrates all of the various features of the model. Previous work on VCSEL modeling has focused on thermal characteristics [11,42,45,46] where the electrical properties are principally based on phenomenological relations. Various optical formulations are either similar [47] or more advanced [48] than the SimWindows model, but again lack fundamental carrier and energy transport physics. One of the key components in the design of a good

VCSEL is the distributed Bragg reflectors (DBRs). There is theoretical [49-51] and experimental [52-54] work on individual DBR structures. However, none have taken the approach of examining how specific DBR designs can influence the overall VCSEL characteristics. This section will examine both the DBR structures and their contribution in complete VCSEL devices.

This section consists of three parts. The first part will discuss the general operation of a VCSEL and compare the best numerical result of a "standard" VCSEL with experimental results. This comparison will show that only when SimWindows uses all of the features in the model, can numerical results approximate experimental results. The second part of this section will focus on the design of the DBR and propose structures that yield better DBR characteristics. The main point from this analysis is that the designs of the n-type and p-type DBRs must be independent from each other. A design that improves one DBR does not necessarily improve the other DBR. The third part of this section will show simulation results of an "improved" VCSEL which incorporates the better DBR structures. Since there are tradeoffs in any design, this part will also present the tradeoffs associated with the improved VCSEL structure.

3.2.1 Standard VCSEL Design

Figure 19 and Figure 20 show band diagrams of a VCSEL structure that this section will refer to as the "standard" structure [55]. Listing 2 in Appendix B gives the SimWindows device file for this structure. Figure 19 shows the equilibrium band diagram while Figure 20 shows the band diagram at 6.0 Volts.

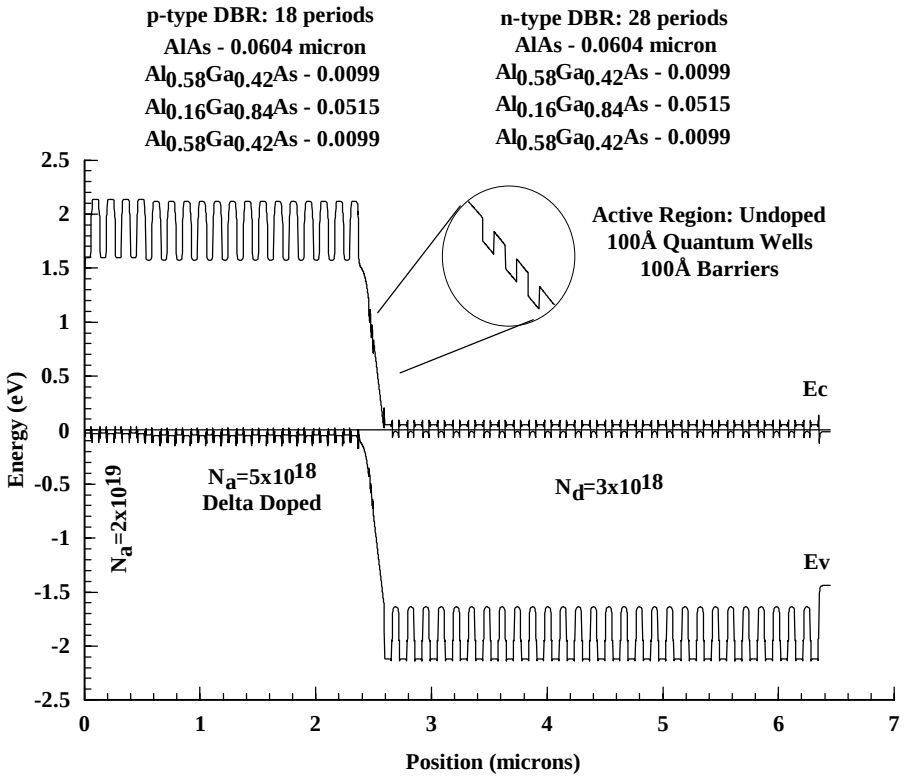

Figure 19 - Equilibrium band diagram for a standard VCSEL

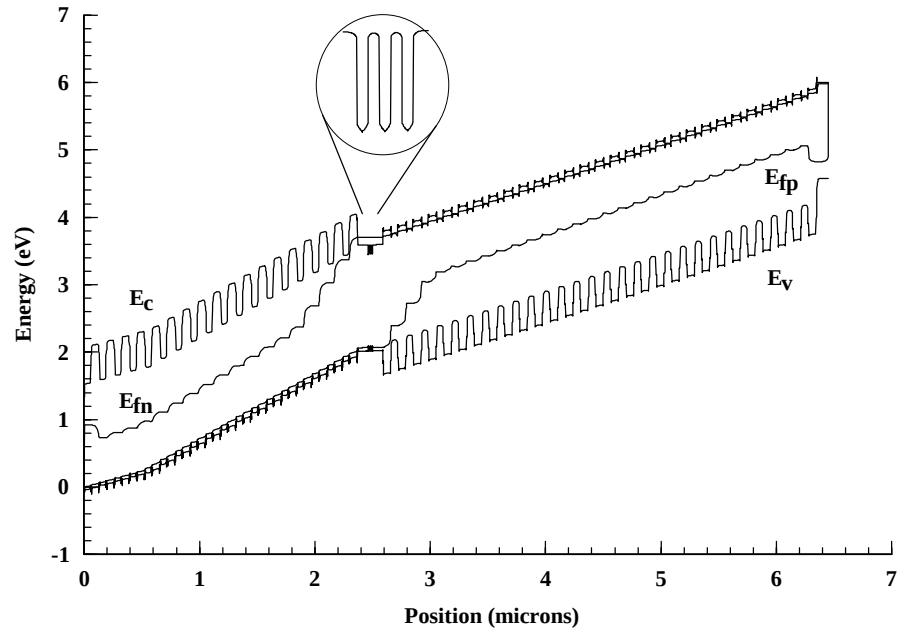

Figure 20 - 6.0 Volt band diagram for a standard VCSEL

A VCSEL works by using two DBRs to reflect light across an active region. DBRs use layers of alternating material such that the optical path length is a quarter of the desired wavelength. This can yield very high reflectivities at specific wavelengths. VCSELs must use high reflectivity DBRs since their active region and overall cavity length are very short. This is in comparison to edge emitting lasers that have a very long active region and as a result can use comparatively small mirror reflectivities. One aspect of the short cavity length of VCSELs is that the spacing between adjacent resonant modes of the cavity is longer than in edge emitting lasers. VCSELs then lase at a single longitudinal mode determined by the optical characteristics of the structure. The VCSEL will emit light when the energy of the resonant wavelength coincides with an energy that the active region amplifies. If there is a mismatch between these energies, then the device will not lase.

The disadvantage of using DBRs is that they are highly resistive and are the main cause of self-heating in VCSELs. Self heating causes the optical characteristics to change because both the refractive index and the band gap are temperature dependent. The change in the refractive index causes the resonant frequency of the cavity to shift at approximately 0.8 Å/K, while the change in band gap causes the gain characteristics of the active region to shift at a rate of approximately 3.3 Å/K [56]. Since the wavelength shifting from these two effects is at different rates, a mismatch will occur between the resonant frequency and the gain characteristics. This mismatch decreases the light output beyond a specific current level. Reducing the resistance of the DBRs is necessary for reducing the heating in VCSELs and minimizing this effect.

The active region of the standard VCSEL in Figure 19 and Figure 20 consists of three undoped 10 nm GaAs quantum wells separated by 10 nm $Al_{0.16}Ga_{0.84}As$ barriers. The DBRs consist of alternating layers of 60.4 nm AlAs and 51.5 nm $Al_{0.16}Ga_{0.84}As$ with the left (top) DBR using 18 periods and the right (bottom) DBR using 28 periods. The DBRs also use 9.9 nm $Al_{0.58}Ga_{0.42}As$ "transition layers" between the thicker layers. These transition regions help reduce the resistance of the DBR by reducing the barriers to current flow in the conduction and valence bands. This configuration of layers yields the highest reflectivity at approximately 846 nm. The greater number of periods for the right DBR gives it a higher reflectivity than the left DBR. These simulations use a reflectivity of 99.9% for the right DBR and 99.75% for the left DBR. The right DBR is doped n-type at a concentration of $3x10^{18}$ cm^{-3}. The left p-type DBR uses two doping sections. The shorter section closer to the contact is doped $2x10^{19}$ cm^{-3} with the longer section doped $5x10^{18}$ cm^{-3}. The left DBR also employs delta doping to reduce its resistance. Delta doping is an extra sheet charge at the interface between materials. The left DBR uses delta doping concentrations of $2.2x10^{12}$ cm^{-2} and $4.5x10^{12}$ cm^{-2} depending on the interface. These doping concentrations are high enough where free carrier absorption is significant, but the SimWindows does not model free carrier absorption. Using the free carrier absorption coefficients in [5] and the computed carrier concentrations from SimWindows, excluding the free carrier absorption in these VCSEL simulations represents approximately a 15% error in the mode gain of the VCSEL.

There are several SimWindows input parameters common to all of the VCSEL simulations in this chapter. These simulations use a waveguide loss of 20 cm^{-1} and a

spontaneous emission factor b of 10^{-3}. The device radius is 3.5 microns which corresponds to an area of 38.5 square microns. The environment radius is 100 microns. These simulations also use a doping and temperature dependent mobility based on the model in [31]. Since the model does not conform to the SimWindows built-in mobility model, the device files in Appendix B incorporates the model directly.

For the thermal boundary conditions at the ends of the laser, the left contact uses a perfect thermal insulator and the right contact uses a finite thermal conductance of 1604.3 W cm^{-2} K^{-1}. This value assumes a small circular heat source in contact with a infinitely wide and infinitely thick layer of GaAs. With these assumptions, the effective thermal conductance per area between the device and the heat sink is given by (113). A discussion of the electrical analog to this equation appears in [57].

$$k_r = \frac{4k}{pr_d} \tag{113}$$

Figure 21 shows a comparison between experimental [55] and numerical results for the standard VCSEL structure. It is important to note that SimWindows can only approximate experimental results when it uses all of the features in the model. In addition to using all three solvers for the main equations, it uses Fermi-Dirac statistics, tunneling current, thermionic emission current, delta doping, temperature and doping dependent mobilities, temperature dependent band gap, temperature dependent thermal conductivity, and a temperature dependent refractive index. If the simulation does not use any one of these features, then the results will change considerably.

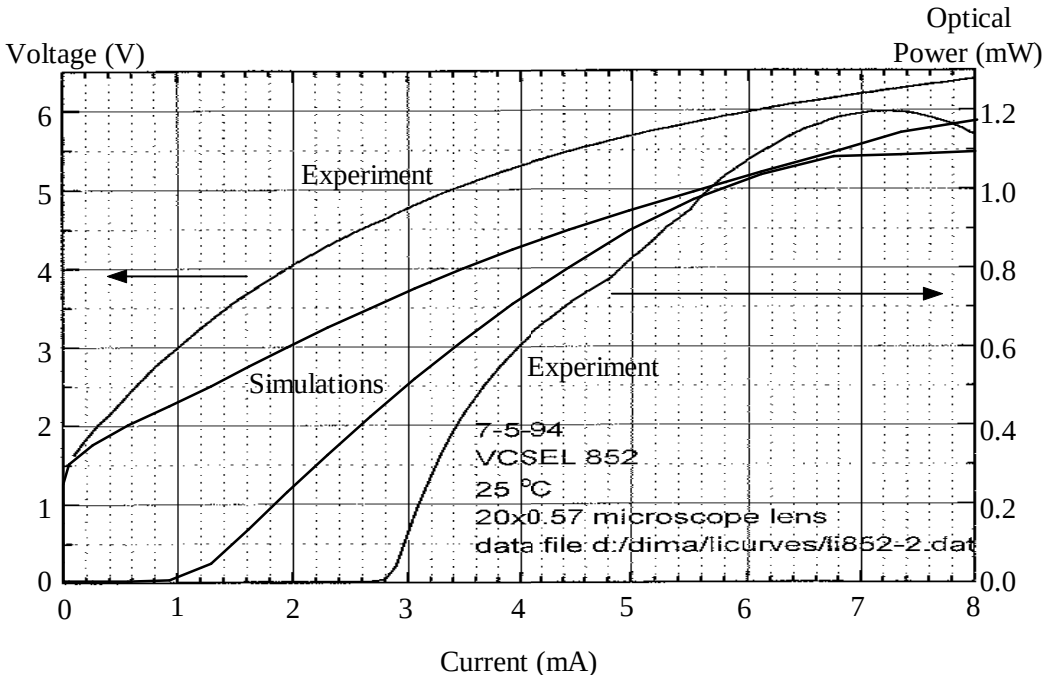

Figure 21 - Experimental and simulated results for the standard VCSEL structure

There are a number of factors that explain the deviation between the experimental results and the simulation. Including free carrier absorption would increase the simulated threshold current. An more accurate quantum well model would improve the coupling between the optical and electrical equations. Both the simulation and the experimental results are on small area devices where two dimensional effects play a role in the device characteristics. The structure of the simulated device is an ideal device obtained from a fabrication sheet. Fabrication variations would yield a device that differs from the specifications. Considering these factors, it is important to examine trends and comparisons in simulation results rather than specific values. The figures and discussion in this chapter will emphasize trends and show comparisons between simulation results.

Figure 22 shows light-current (LI) plots for simulations using different physical

models. The curve labeled "Delta Doping, Wavelength Shift" is the same numerical result shown in Figure 21 except on a wider current scale. Curves labeled "No Wavelength Shift" use a temperature independent refractive index. This keeps the lasing wavelength constant, but the temperature dependent band gap still causes the rollover characteristic where the optical power decreases with increasing current. Since both the band gap and the lasing wavelength shift towards lower energy, using a constant lasing wavelength in the simulations actually causes the rollover at a lower current level.

Delta doping is one method to reduce the resistance of the p-type DBR. The characteristics in Figure 22 improve when using delta doping because the VCSEL consumes less electrical power for a given current. This leads to less heating and better optical characteristics. The next section will discuss more aspects of the DBR design.

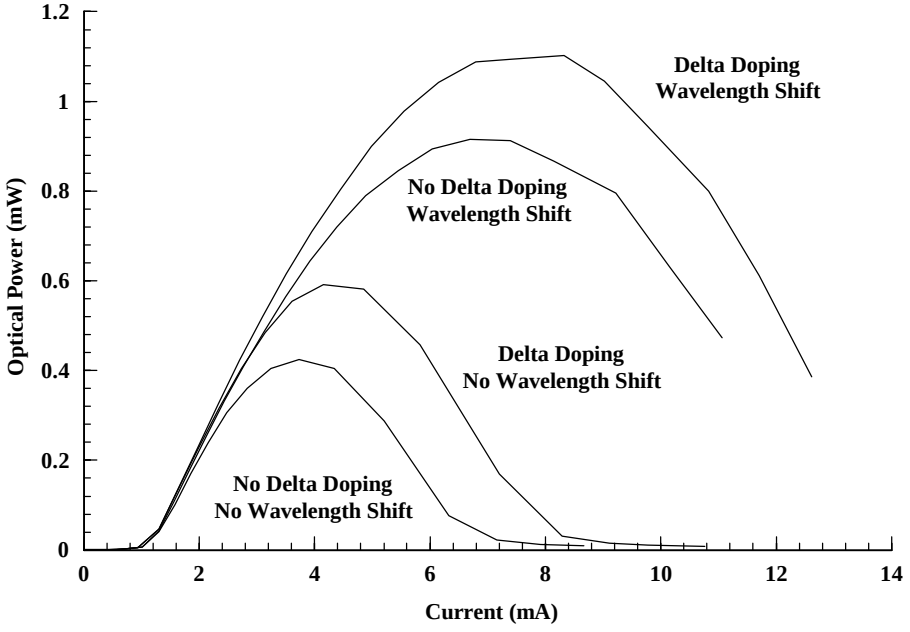

Figure 22 - LI plots for combinations of delta doping and wavelength shifting

SimWindows can also generate light-current-voltage (LIV) characteristics for different operating conditions. Figure 23 shows these characteristics for different environment temperatures. Not only does the light output decrease at higher temperatures, the threshold current also increases. This again reflects the interaction between the optical equations and the thermal equations. Figure 24 shows the corresponding shift in wavelength versus the injected power into the VCSEL for different environment temperatures.

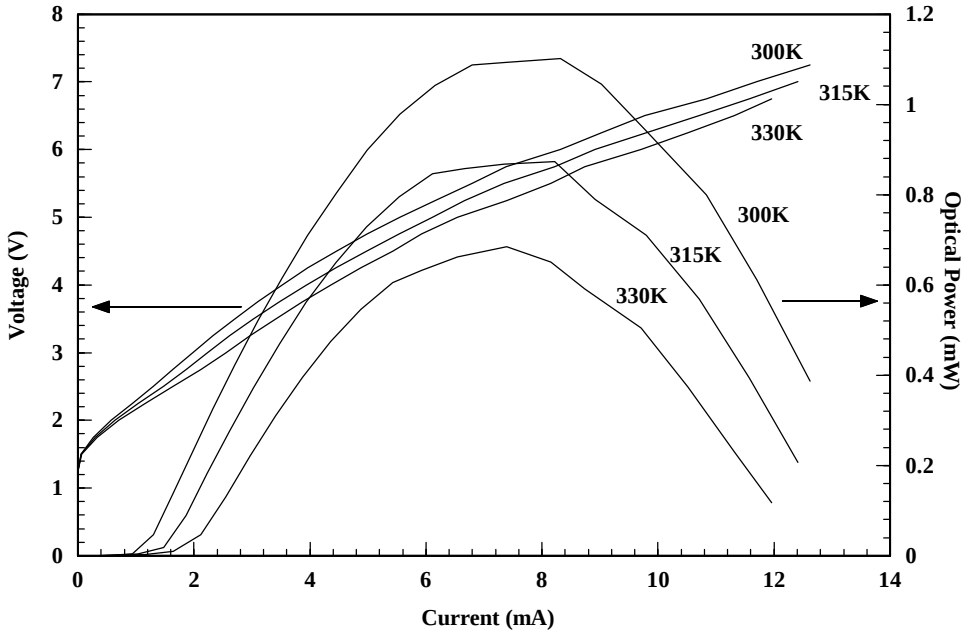

Figure 23 - LIV characteristics for the standard VCSEL at different environment temperatures

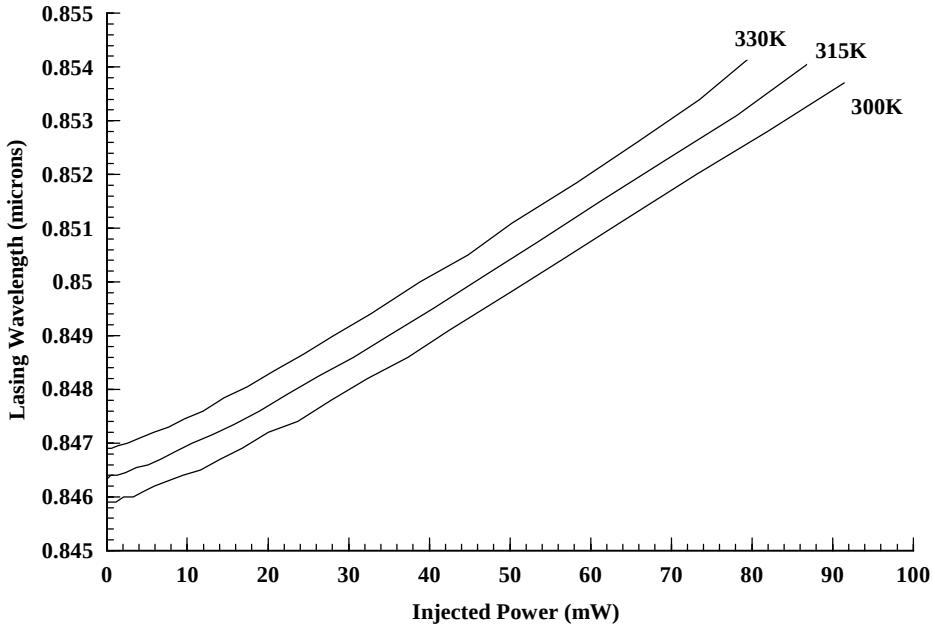

Figure 24 - Wavelength versus injected power at different environment temperatures

3.2.2 DBR Design

The design of the DBR is critical in determining the characteristics of the laser. Since the DBR uses a periodic structure, it is useful to analyze just one period of the DBR and then simulate the complete structure. As stated in the previous section, both DBRs in the standard VCSEL structure use 9.9 nm transition layers of $Al_{0.58}Ga_{0.42}As$. These do help reduce the resistance of the DBR, but it is not clear that a constant concentration of 58% aluminum is the optimum concentration. It is also not clear that this transition region has the same impact on the resistance in both the n-type and p-type DBRs. Various types of SimWindows simulations can address these issues.

Figure 25 shows the conduction band for 1.5 periods of an n-type DBR. The inner region uses 16% aluminum and the outer region uses pure AlAs. Listing 3 in Appendix B shows the device file for this structure. The aluminum concentration of the 9.9 nm transition region ranges from 20% to 100%. The bias on this structure is

0.25 Volts and Figure 25 shows the direction of electron flow. This figure shows that considerable barriers to electron flow exist at an aluminum concentration of 58% that the standard VCSEL structure uses. The lowest effective barrier height occurs at approximately 30% aluminum. Figure 26 shows a similar graph for the valence band. Note that this figure plots the valence band versus hole energy. Therefore holes flow down the valence band profile. Listing 4 in Appendix B has the device file for this p-type structure. Again the bias on the structure is 0.25 Volts. It is clear that the conduction band is considerably different from the valence band. In the case of holes the minimum barrier height does occur at approximately 60% aluminum which the standard VCSEL structure uses.

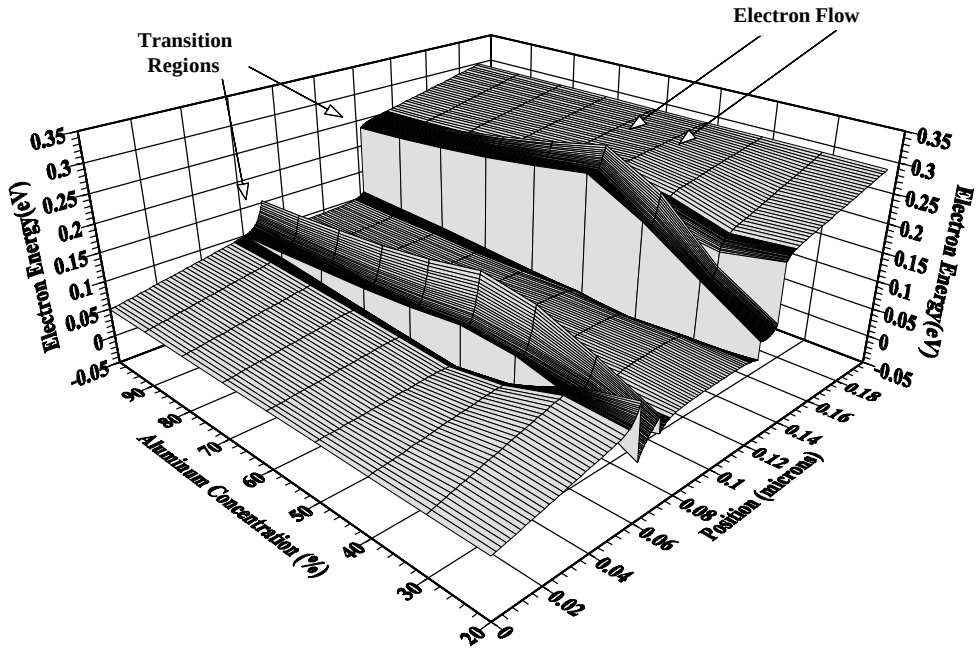

Figure 25 - Conduction band of 1.5 periods of a DBR for different transition layer concentrations

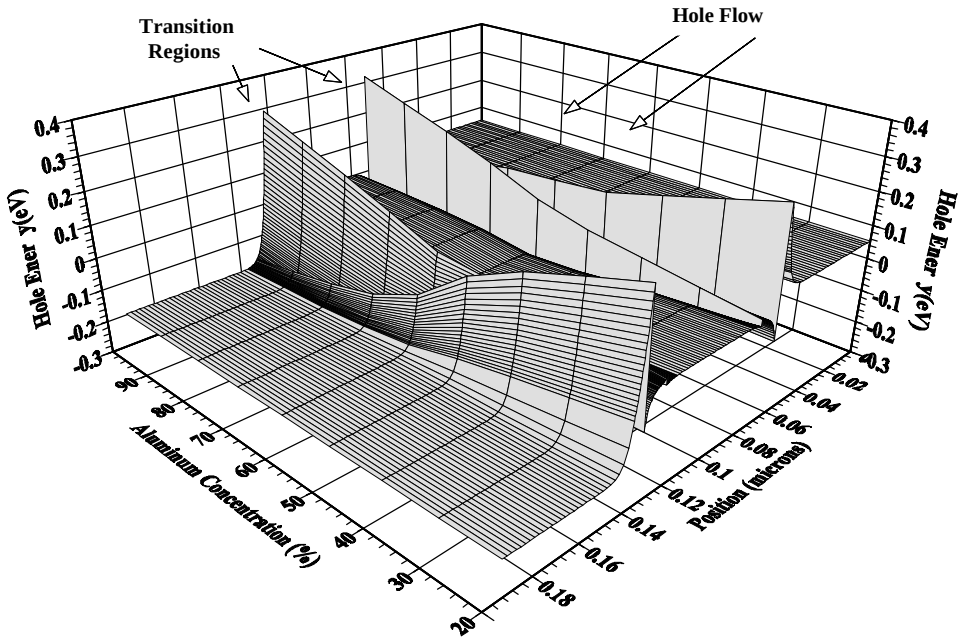

Figure 26 - Valence band of 1.5 periods of a DBR for different transition layer concentrations (note that z axis is hole energy)

Figure 27 again makes clear that the conduction and valence band profiles have different effects on the current. This figure shows the electron current density through the structure in Figure 25 and the hole current density through the structure in Figure 26 as a function of the transition layer aluminum concentration. The peak electron current occurs at 30% aluminum while the peak hole current occurs at 60% aluminum. Even just using a simple design where the transition layer aluminum concentration is constant, the design of the n-type and p-type DBRs should be different in order to reduce the resistance of both DBRs.

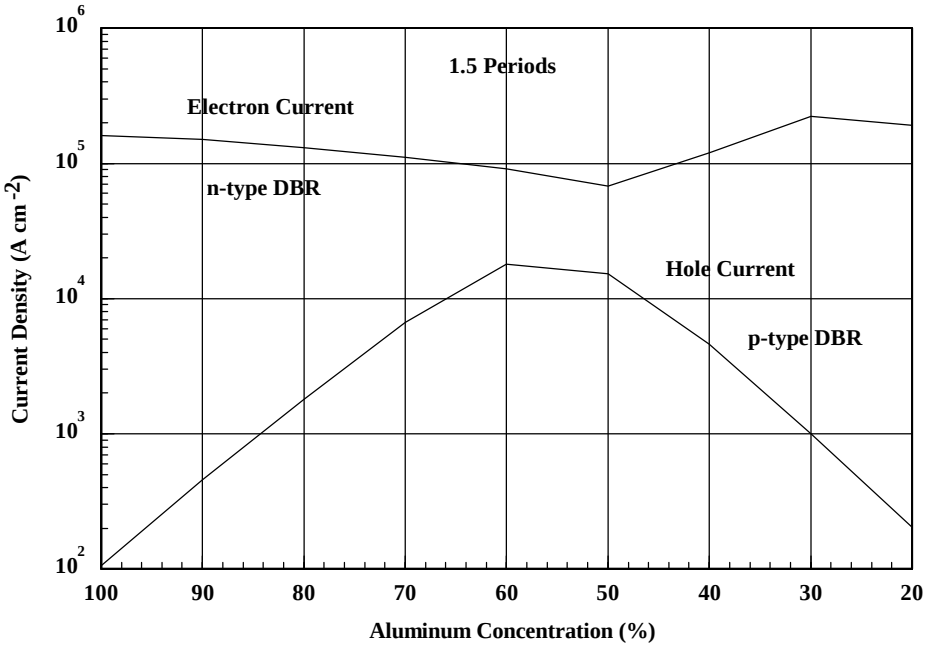

Figure 27 - Electron and hole current through 1.5 periods of an n-type and p-type DBR for various transition layer concentrations

Another question about DBR design is what other types of transition regions can yield yet smaller resistances. A second typical design is to use a linearly graded aluminum concentration rather than a constant intermediate concentration.

Figure 28 compares the conduction bands and quasi-fermi levels for 1.5 periods of an n-type DBR using a constant 30% aluminum transition layer versus a 100% to 16% linearly graded aluminum transition layer. Note that the conduction band in the 30% Al plot is a cross sectional slice of the surface plot in Figure 25. This figure clearly shows that the effective barriers to electron flow are greater for the linearly graded region than for the constant 30% region. This results in a larger voltage drop across the transition regions as illustrated by the larger change in quasi-fermi level in the linearly graded case than in the constant 30% case. The cause of the higher barriers in the linearly graded case is the decrease in the electron affinity between

100% and 50% aluminum concentration. When grading between 100% and 16% aluminum, the electron affinity actually decreases until the aluminum concentration reaches 50% and then the electron affinity increases again. This decrease produces the higher barriers seen in both Figure 25 and Figure 28. An issue is whether this same result is true for p-type materials.

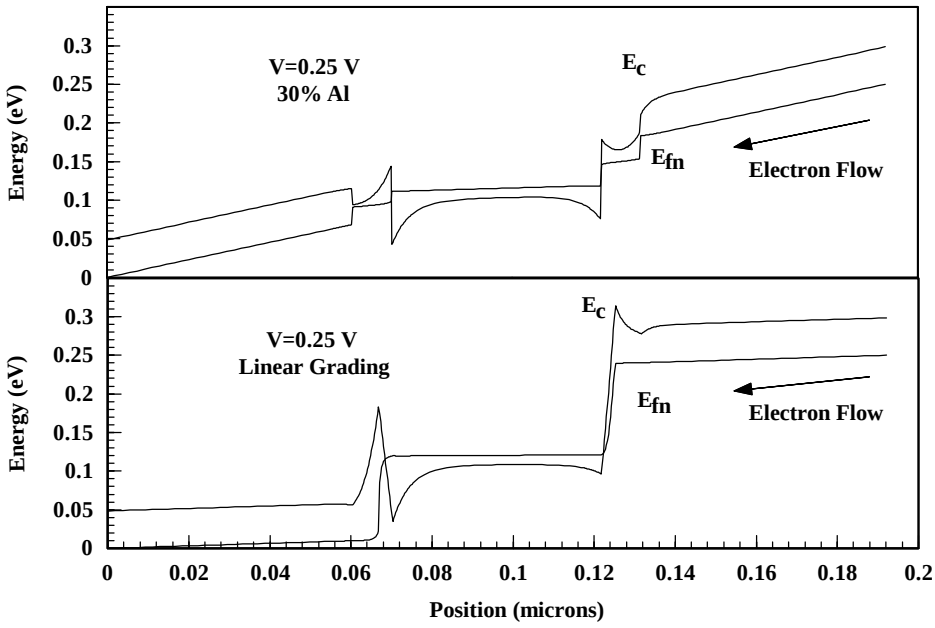

Figure 28 - Conduction bands and quasi-fermi levels for 1.5 periods of an n-type DBR using 30% and linear graded transition regions

Figure 29 compares the valence bands and quasi-fermi levels for 1.5 periods of a p-type DBR using a constant 60% aluminum transition layer versus a 100% to 16% linearly graded aluminum transition layer. Again the valence band in the 60% Al plot is a cross sectional slice of the surface plot in Figure 26 except that Figure 29 plots the electron energy. In this case, the linear grading drastically reduces the barrier height for holes. The combination of the electron affinity and the band gap favors linear

grading over a constant transition layer. These two figures underscore the fact that a design which improves one DBR may actually be detrimental to the other DBR.

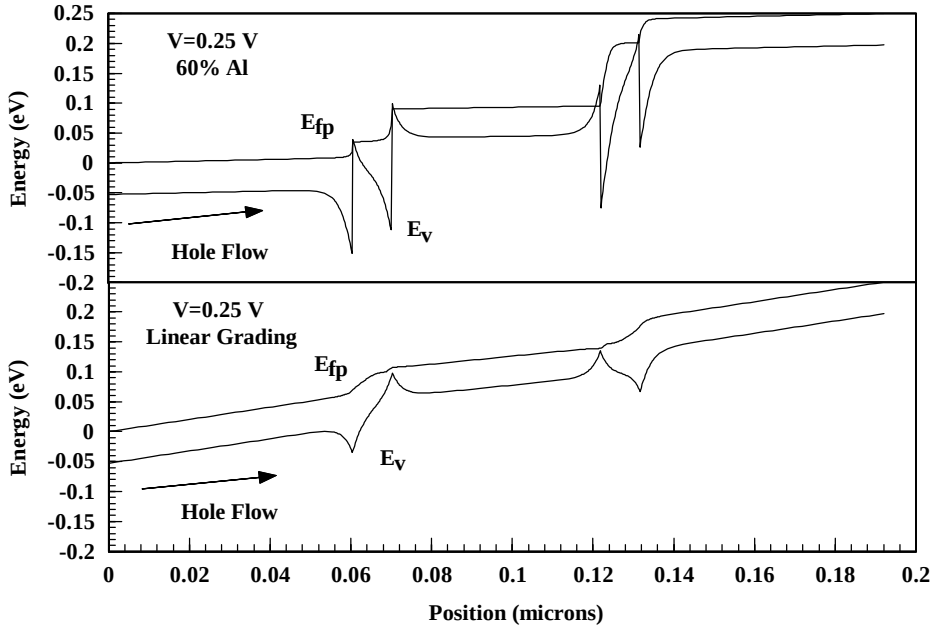

Figure 29 - Valence bands and quasi-fermi levels for 1.5 periods of a p-type DBR using 60% and linear graded transition regions

The next step in this DBR analysis is to examine how the changes in the design of each period relates to improved electrical characteristics of the entire DBR. This section will refer to the "improved" p-type DBR as a structure that uses a linearly graded transition layer while the "improved" n-type DBR uses a constant 30% aluminum transition layer.

Figure 30 compares the simulated IV characteristics for the standard and improved designs of a 28 period n-type DBR. Listing 5 in Appendix B has the device file for the complete n-type DBR. The improved design reduces the resistance by a factor of 3.3 from $7.69 \times 10^{-5}\ \Omega\ cm^2$ to $2.33 \times 10^{-5}\ \Omega\ cm^2$, but this figure shows that both

designs still rely on tunneling through thin potential barriers because simulations without tunneling increases the resistance. Figure 28 shows that these barriers are present with a 30% aluminum transition region.

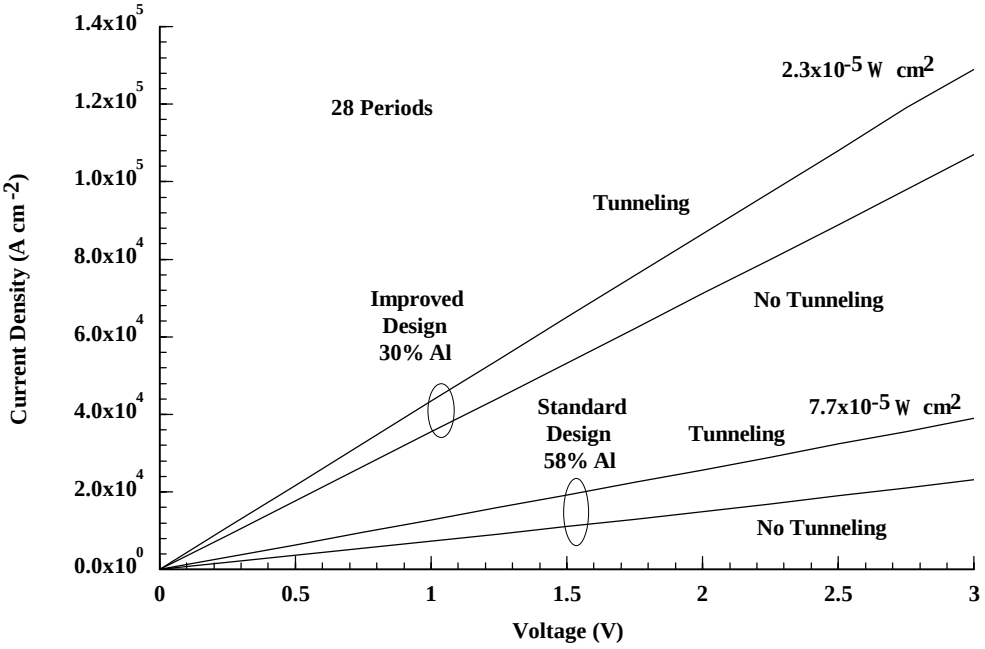

Figure 30 - IV comparisons of the improved versus standard n-type DBR design

Figure 31 shows similar IV characteristics for a 14 period p-type DBR. Listing 6 in Appendix B has the device file for the complete p-type DBR. These characteristics differ from those in Figure 30 in two ways. First, the reduction in resistance is by a factor of 7.1 from $1.51 \times 10^{-4}\ \Omega\ cm^2$ to $2.11 \times 10^{-5}\ \Omega\ cm^2$. Second, the improved p-type DBR design relies much less on tunneling current than both the standard p-type DBR design as well as either of the n-type DBR designs. Simulation results in Figure 31 for the improved design show only a slight increase in resistance when neglecting tunneling current. This is a direct result of the linear grading region having a strong effect on the potential barriers as shown in Figure 29.

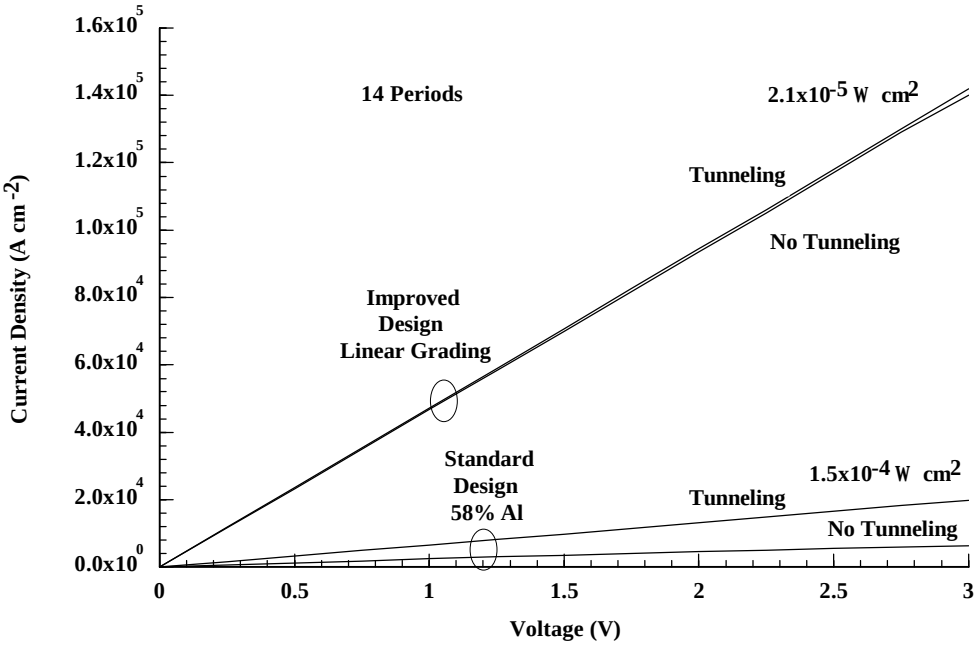

Figure 31 - IV Comparisons of the improved vs. standard p-type DBR design

3.2.3 Improved VCSEL Design

The last step in this analysis is to integrate the two improved DBR designs into a VCSEL structure and simulate the device. Listing 7 in Appendix B has the SimWindows device file for the improved VCSEL design. One aspect of the new DBR designs not mentioned in the previous section is the change in the optical characteristics resulting from the new transition layers. The linear grading of the transition layer in the p-type DBR does not have a significant effect on the reflectivity of the DBR. The shift from a 58% to a 30% aluminum concentration in the n-type DBR transition layer does shift the reflectivity of the DBR to longer wavelengths. To counter this shift, the n-type DBR in the improved VCSEL uses a 9.43 nm instead of a 9.9 nm transition region. This keeps the optical path length of each period in the improved DBR the same as the standard DBR, and forces the resonant frequency of the cavity back to 846 nm. This change will have a slight but noticeable detrimental

effect on the thermal characteristics of the improved VCSEL.

Figure 32 compares the LIV characteristics of the standard VCSEL structure with those of the improved VCSEL structure. The figures shows that by using the designs from the previous section, the improved device can generate higher peak optical powers than the standard device. This is a result of the lower resistance in the DBRs. At any given current, the device consumes less electrical power, there is less heating, and higher optical power.

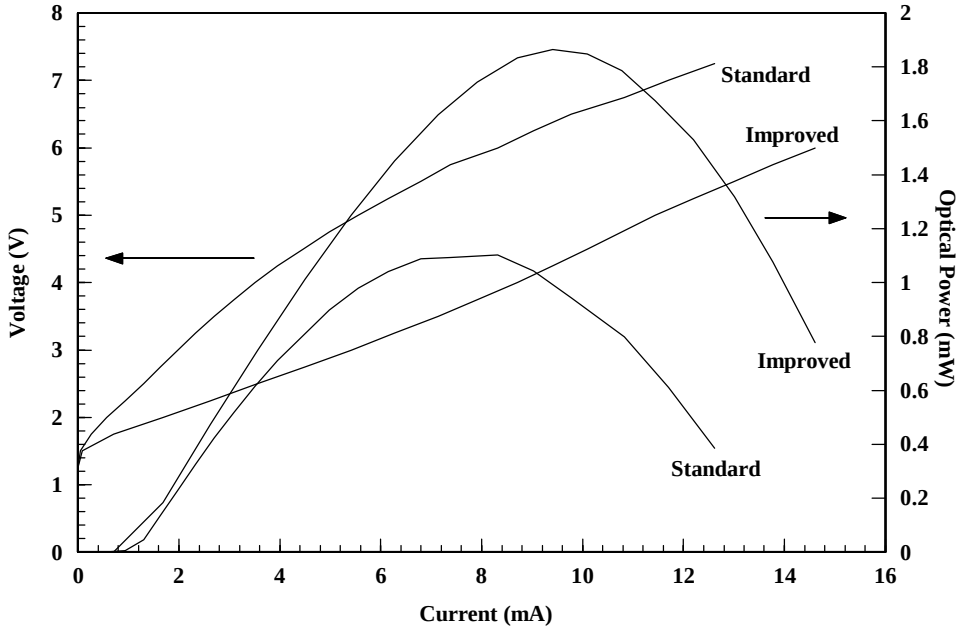

Figure 32 - LIV characteristics for the standard and improved VCSEL

Figure 33 compares the optical power versus the electrical power for the standard and improved VCSEL device. The peak optical power for both devices occurs at approximately the same electrical power. This is a result of the direct relationship between the temperature and the power injected into the device. The thermal effects on the optical characteristics are almost identical in both devices, but

for a given power injected into the device, the improved VCSEL uses more current at a lower voltage yielding greater emitted optical power.

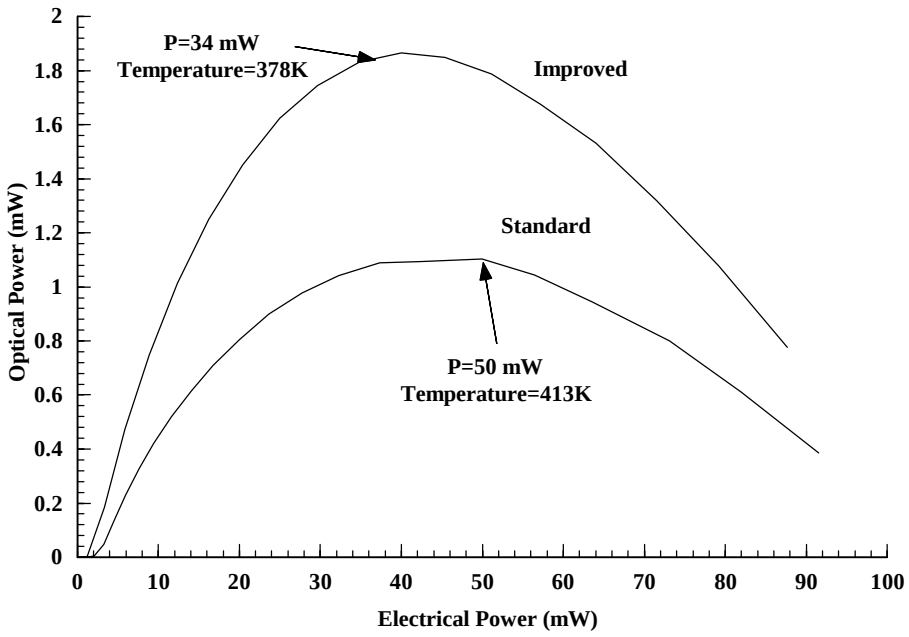

Figure 33 - Optical vs. electrical power for the standard and improved VCSEL

Figure 34 shows the lasing wavelength versus the injected electrical power. This figures shows one of the detrimental effects of using the improved VCSEL. Since the improved device uses different transition layers than the standard device, the improved device actually heats more at the same power level due to the change in the thermal conductivities of the transition layers. This means that the wavelength of the improved device shifts more with power than the standard device. At an operating power of 40 mW where both devices emit the highest optical power, the change in wavelength is less than 1%.

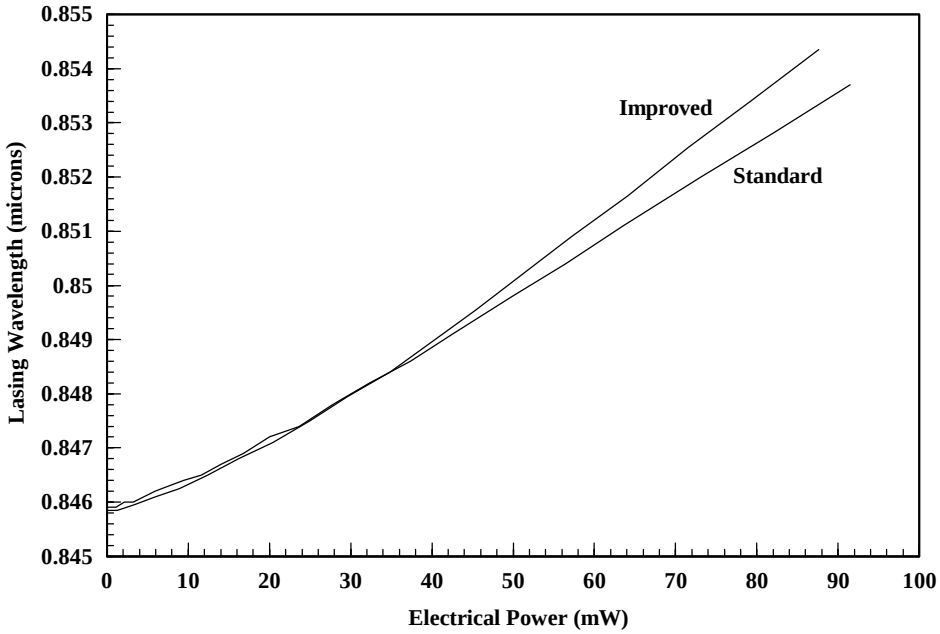

Figure 34 - Lasing wavelength vs. power for the standard and improved VCSEL

Figure 35 compares the lattice temperature profiles of the standard and improved VCSEL structures. The optical power emitted by each device is 1.1 mW, but the improved device can emit this power at a much lower voltage. As a result, the electrical power dissipated by the device is less which yields a lower temperature.

This analysis was by no means a complete analysis of VCSEL structures, but it served to demonstrate the tight coupling between the electrical, optical, and thermal equations. SimWindows can help analyze how specific design changes can affect both the individual component of a device as well as the complete device structure.

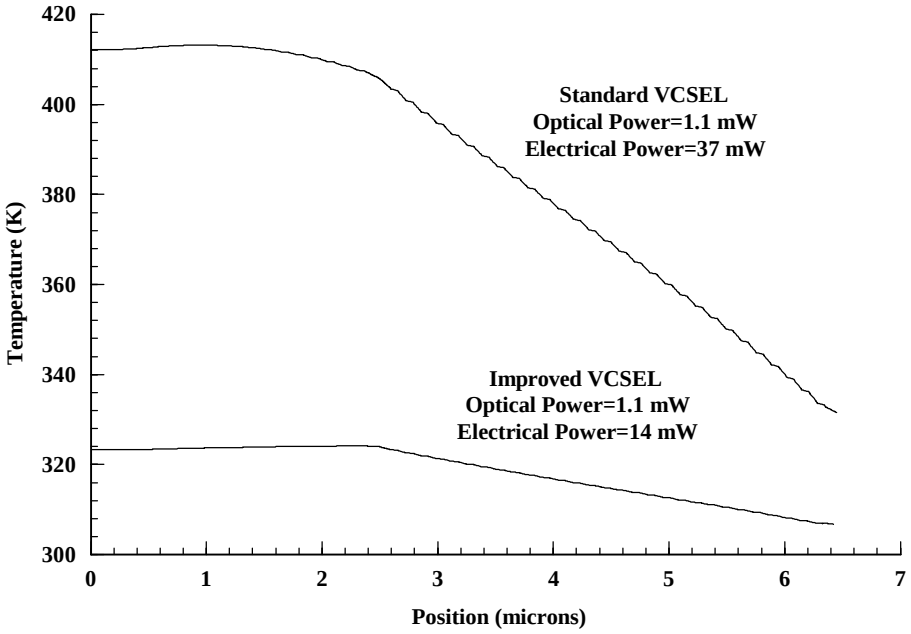

Figure 35 - Temperature profiles for the standard and improved VCSEL at 1.1 mW optical power

3.3 Quantum-Well Solar Cell

The previous section described the VCSEL device where SimWindows uses the Single Temperature Model to simulate lattice heating and the resulting thermal effects. This section will describe simulation results of a quantum-well solar cell. These results will use the Hot Electron Model where the electron temperature deviates from the constant lattice and hole temperatures. It has been proposed [58] that hot electrons might serve to improve the maximum efficiency of solar cells. Since recent measurements [59] have shown that the energy relaxation lifetime can be considerably longer in quantum wells than bulk material, this section will investigate how hot electrons might improve the characteristics of a simple multi-quantum-well solar cell.

Figure 36 shows the integrated AM 1.5 solar spectrum. This figure is the integral over wavelength of the intensity data in [24]. This converts the spectrum from

units of mW cm^{-2} $micron^{-1}$ to mW cm^{-2} which is compatible with SimWindows. Figure 37 shows the band diagram of the multi-quantum well solar cell that is illuminated from the left using the spectrum in Figure 36. Listing 1 in Appendix B has the device file for this section. The principle of this device is to generate hot electrons in the quantum wells. Since the hot electrons have a greater average energy, more of them can escape out of the quantum wells and drift towards the contacts. This reduces the recombination in the quantum wells, yields a higher short circuit current, and increases the maximum power that the solar cell can generate. This is an idealized description, and there are some complications that SimWindows can help analyze.

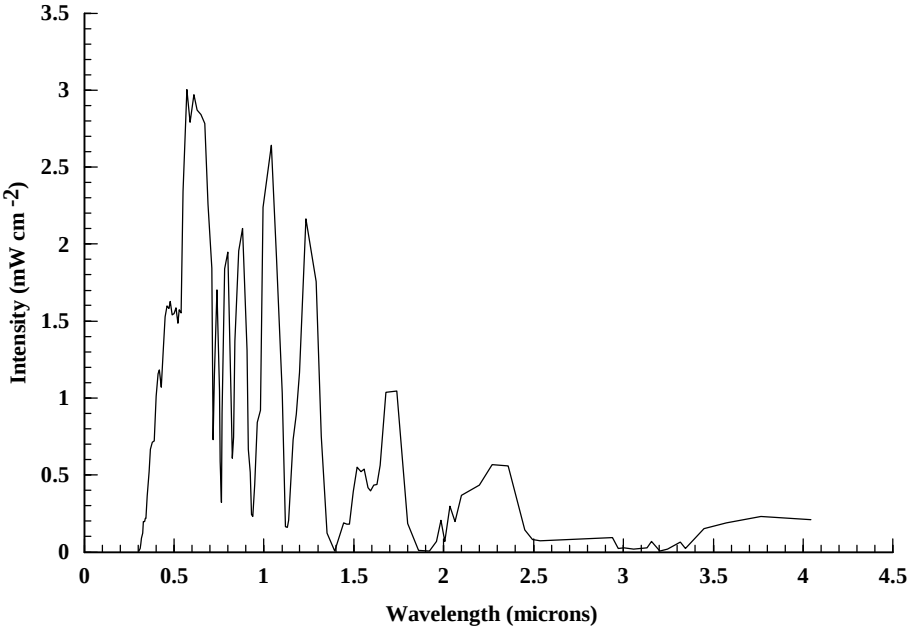

Figure 36 - Integrated AM 1.5 solar spectrum.

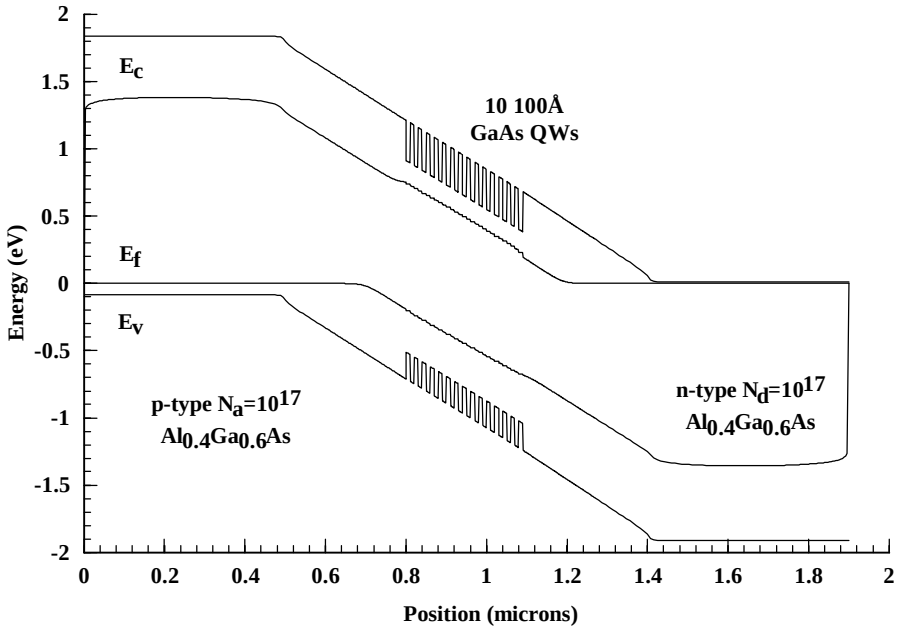

Figure 37 - Band diagram for a multi-quantum well solar cell illuminated from the left with AM 1.5 under short circuit conditions

Figure 38 compares the electron concentration when illumination is from the left and the right. There is a lower minority electron concentration near the left contact when illumination is from the right because the absorbing quantum wells reduces the light intensity. This is in comparison to left illumination which generates minority electrons before the quantum wells reduce the light intensity. Figure 37 and Figure 38 do not use the SimWindows hot electron model. Enabling this model will cause the electrons in the quantum wells to gain a higher energy.

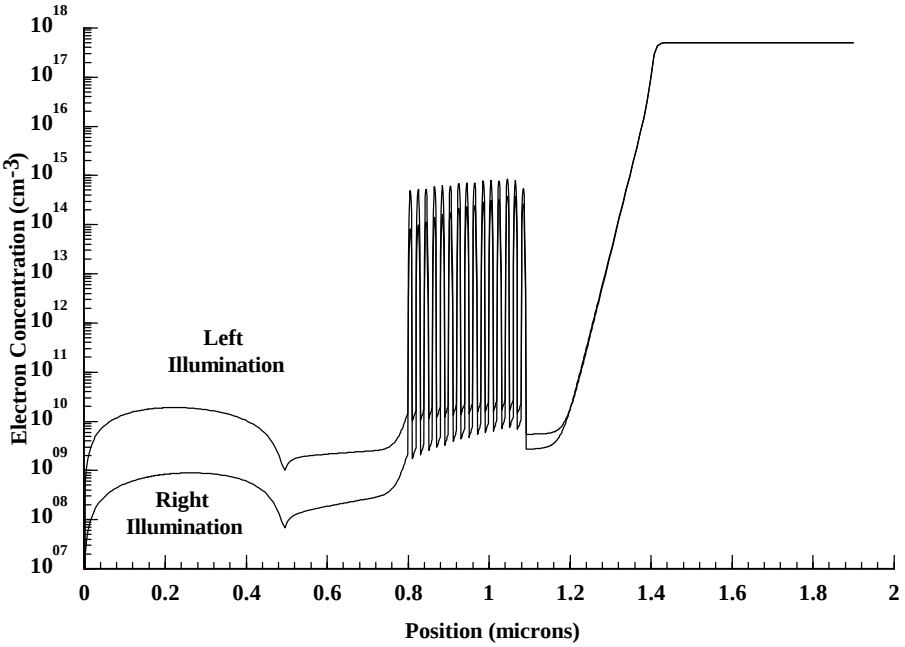

Figure 38 - Electron concentration for left and right illumination under isothermal conditions

Figure 39 compares the computed electron temperature for left and right illumination using the SimWindows hot electron model. Figure 40 shows the corresponding electron concentration. This device uses a 10^{-9} s energy relaxation lifetime for the quantum wells and a 10^{-12} s lifetime for bulk regions. These lifetimes will demonstrate the effect of longer lifetimes in the quantum wells than in the bulk regions. The device also uses a short 10^{-16} s lifetime within 0.2 microns of each contact. This short lifetime models the effect of a contact by causing the electron temperature to smoothly return to 300K at the contacts. It is clear that when comparing Figure 40 to Figure 38, the electron concentration in the quantum wells is significantly less in the hot electron case than in the isothermal case. Since the hot electron model allows the electrons in the quantum wells to achieve a higher temperature, more of them are thermionically emitted over the top of the quantum

wells. To understand the origin of the temperature profiles in Figure 39, it is useful to overlap the temperature and the electron concentration. Figure 41 shows the overlap of the electron temperature and concentration for left illumination.

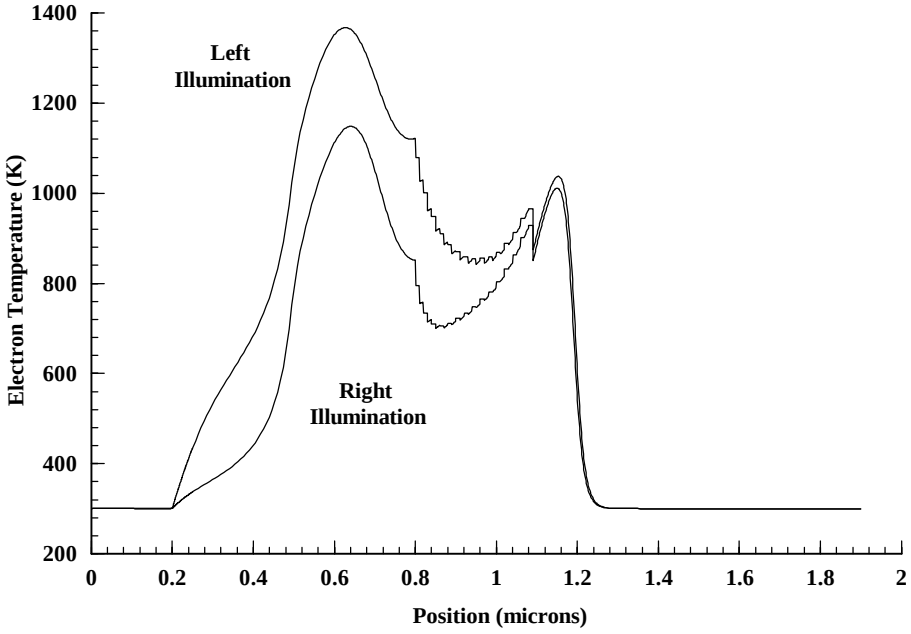

Figure 39 - Electron temperature for left and right illumination

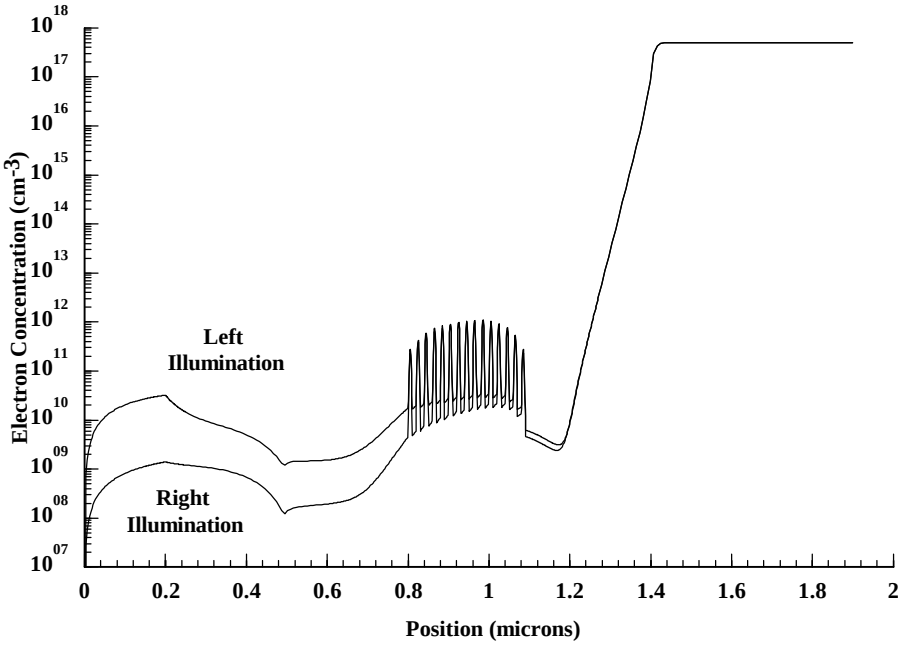

Figure 40 - Electron concentration for left and right illumination using hot electron model

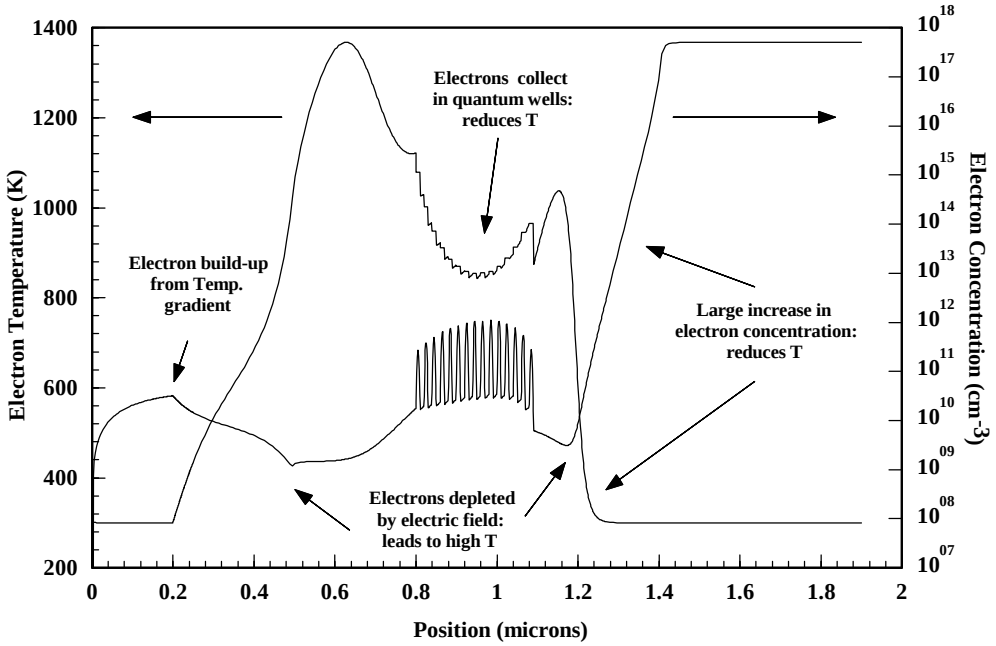

Figure 41 - Overlap of electron temperature and concentration for left illumination

It is important to remember that there is an inverse relationship between the electron concentration and the electron temperature. Since the temperature is a measure of the electrons average energy, in regions with high electron concentrations, the electrons need a significant amount of energy to raise their temperature. In regions with low electron concentrations, a small amount of energy will raise their temperature. In Figure 41, the concentration at 0.6 and 1.2 microns is low because the electric field in the intrinsic region accelerates the electrons. This leads to an increase in the temperature at these locations. Quantum wells serve to reduce the temperature because a large number of electrons still remain in the quantum wells. Towards the n-type side of the device, the concentration between 1.2 and 1.4 microns grows by several orders of magnitude which reduces the temperature back to 300K. The last item to note about Figure 41 is that there is large temperature gradient between 0.2 and 0.6 microns. This gradient causes electrons to diffuse to the left and build up near the left contact.

It may seem that if hot electrons can escape out of the quantum wells and drift towards the contacts, there will always be an increase in the short circuit current of the solar cell. This is not the case. With left illumination, the short circuit current decreases from 11.5 mA cm^{-2} to 10.0 mA cm^{-2}. With right illumination the short circuit did increase from 10.7 mA cm^{-2} to 12.1 mA cm^{-2}. The answer to this anomaly lies in Figure 39 and Figure 40. As stated above, the temperature gradient between 0.2 and 0.6 microns causes electrons to diffuse toward the left contact. These electrons are diffusing in the opposite direction than those drifting through the intrinsic region. In certain cases, these "wrong way" electrons actually counter any gains in the short

circuit current resulting from fewer carriers in the quantum wells. This is the case with left illumination. With right illumination, both the minority electron concentration near the left contact and the temperature gradient toward the left contact are less than with left illumination. This reduces the effect of the "wrong way" electrons enough for the hot electrons in the quantum wells to increase the short circuit current.

Figure 42 compares the IV curves for the solar cell for left and right illumination using the hot electron model. With hot electrons, the maximum power for left illumination is 10.8 mW cm^{-2} while the maximum power for right illumination is 13.3 mW cm^{-2}. Since right illumination minimizes the effect of the wrong way electrons, the maximum power available is greater than for left illumination. This figure also shows the IV curve for left and right illumination using the standard isothermal model. Under isothermal conditions, the maximum power for left illumination is 12.1 mW cm^{-2} while the maximum power for right illumination is 11.3 mW cm^{-2}. Despite the maximum power for each case, both hot electron cases produced higher open circuit voltages than either of the isothermal cases.

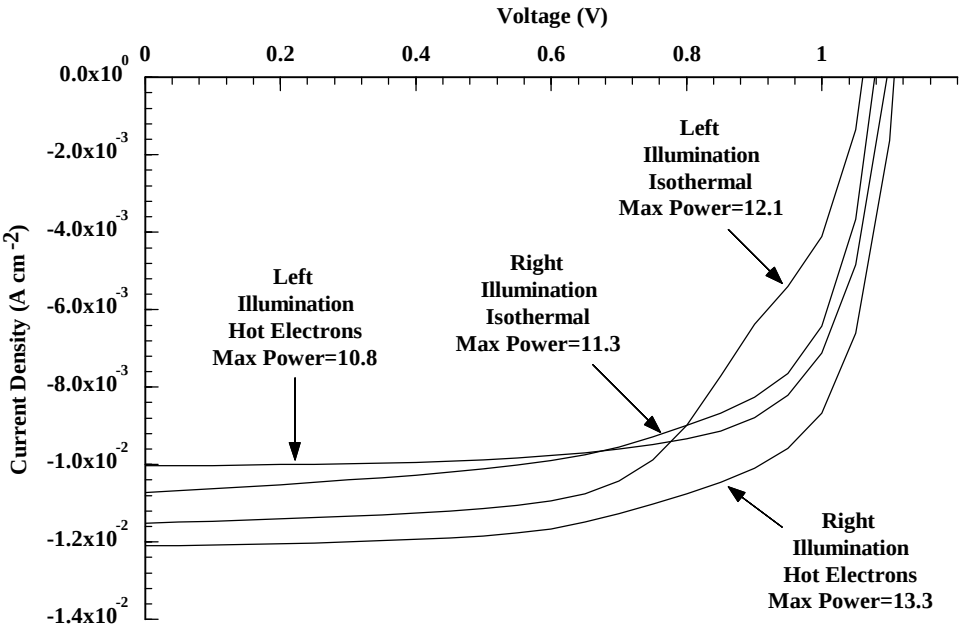

Figure 42 - IV curves for left and right illumination using hot electrons